AIMS Materials Science, 10(6): 1090–1104.
DOI: 10.3934/matersci.2023058
Received: 22 July 2023
Revised: 05 September 2023
Accepted: 15 September 2023
Published: 04 December 2023

http://www.aimspress.com/journal/Materials

Research article

Enhancing Co_3O_4 nanoparticles: Investigating the impact of nickel doping and high-temperature annealing on $NiCo_2O_4$/CoO heterostructures

Leydi J. Cardenas F.[1,2], Josep Ma. Chimenos[3], Luis C. Moreno A.[4], Elaine C. Paris[5] and Miryam R. Joya[6,*]

[1] Facultad de Ingeniería-Departamento de Ingeniería Mecánica y Mecatrónica, Universidad Nacional de Colombia sede Bogotá, Bogotá, Colombia
[2] Departamento de Ingeniería Mecánica y Mecatrónica, Universidad de América, Bogotá, Colombia
[3] Departamento de Ciencia de Materiales y Química Física, Universitat de Barcelona, Barcelona, Spain
[4] Laboratorio de aplicaciones fisicoquímicas del estado sólido AFES, Departamento de Química, Universidad Nacional de Colombia-sede Bogotá, Bogotá, Colombia
[5] Nanotechnology National Laboratory for Agriculture (LNNA), Embrapa Instrumentacção, XV de Novembro st, 1452, 13560-970, São Carlos, São Paulo, Brazil
[6] Departamento de Física, Facultad de Ciencias, Universidad Nacional de Colombia-Bogotá, Carrera 30 Calle 45-03, 111321, Bogotá, Colombia

* **Correspondence:** Email: mrinconj@unal.edu.co; Tel: +57-1-3165000.

Abstract: In this study, we investigated the phase transition of cobalt spinel (Co_3O_4) nanoparticles into $Co_{3-x}Ni_xO_4$/CoO heterostructures by introducing varying amounts of nickel (x = 0.0–0.16) and subjecting the particles to high annealing temperatures of 1000 ℃. X-ray diffraction (XRD) analysis confirmed the $Co_{3-x}Ni_xO_4$CoO structure for all samples. Transmission electron microscopy (TEM) provided further insights into the phase or heterostructure of the samples after annealing, revealing the arrangement of the two phases. Fourier-transform infrared spectroscopy measurements demonstrated a band shift around 537 cm^{-1} with increasing Ni content, while ultraviolet-visible (UV-Vis) measurements indicated the energy band (*Eg*). Significant morphological changes were observed in scanning electron microscope (SEM) measurements at 0.16 Ni, displaying irregular agglomerates. Our findings suggest that introducing Ni into the Co_3O_4 structure and increasing the annealing temperature to 1000 ℃ can lead to the formation of a heterostructured system. Furthermore, our study's significance is highlighted

by the streamlined synthesis of $NiCo_2O_4$/CoO using the sol-gel method followed by calcination. This departure from complex techniques provides an efficient route to acquiring the $NiCo_2O_4$/CoO system, a promissory material for advancing supercapacitor research.

Keywords: cobaltite; $NiCo_2O_4$; heterostructure; annealing temperature; Ni; TEM

1. Introduction

It is essential to find urgent solutions to create new energy sources and innovative conversion and storage technologies, due to the scarcity of fossil fuels and environmental concerns associated with conventional technologies [1]. Nickel cobaltite ($NiCo_2O_4$) exhibits superior electrochemical activity and significantly higher electrical conductivity, surpassing pure Co_3O_4 [2] and NiO by at least two orders of magnitude. This remarkable characteristic enables it to achieve exceptional specific capacitance. Recent studies have proposed that nickel cobaltite exhibits a broader range of redox reactions, attributed to the involvement of nickel and cobalt ions, setting it apart from monometallic nickel and cobalt oxides. Furthermore, the presence of multiple oxidation states and diverse nanostructures in nickel cobaltite spinel holds promise for enhanced charge storage capacity [1].

Several researchers have explored the hybridization of spinel cobalt oxide with various elements, including Cu [3], CeO_2 [4], CdS [5], V and F [6], which has led to improvements in its physical properties, capacitive performance and sensitivity to different gases. However, nickel cobaltite stands out for its promising properties. For instance, Keerthana et al. [7] demonstrated that doping Co_3O_4 with Sn enhanced its catalytic performance. Abdallah et al. [8] introduced Sm and Er into Co_3O_4 nanoparticles, determining maximum solubility doping values and analyzing the compound's magnetic behavior with potential applications in data storage. Li et al. [9] developed Co_3O_4/Zn rechargeable aqueous batteries, laying the foundation for high-capacity cathode functionality.

$NiCo_2O_4$ is a material with broad applications, particularly in the context of heterostructures. For instance, the literature reveals the development of electrocatalytic heterostructures by combining MoS_2 nanosheets with a hollow sphere of $NiCo_2O_4$ on a Ti mesh. These heterostructures are distinguished by their heterogeneous nanointerface between $NiCo_2O_4$ and MoS_2, resulting in a highly efficient electrocatalyst [10]. Multiple samples have been assessed, and the results demonstrate that the $NiMoO_4$@$NiCo_2O_4$/NF heterostructural electrode exhibits outstanding catalytic performance [11]. Furthermore, it is worth noting the vertical cultivation of $NiCo_2O_4$ nanosheets on a Ti mesh, which has led to the development of a $NiCo_2O_4$/Ti catalyst with exceptional electrochemical reactivity, promoting electron transfer across the $NiCo_2O_4$/Ti interface [12]. In other studies, it has been reported that nickel cobaltite ($NiCo_2O_4$), in contrast to NiO and Co_3O_4, exhibits a higher density of electroactive sites and conductivity at least two orders of magnitude greater [1]. These hybrid materials, known as transition metal oxide compounds, have been extensively studied for various applications, particularly in the areas of electrochemical efficiency [13] and advanced energy storage [14], manufacturing of high-performance devices, absorbent materials [15], electrocatalysis [16], sensors, etc. Specifically, the bimetallic oxide $NiCo_2O_4$ has been studied thanks to the control over its morphology. Nano size geometries can allow greater control of the chemical or physical behavior of their properties, various forms of synthesis [17], heterogeneous interface, among others. According to the literature, the

synthesis of the NiCo/NiO/$NiCo_2O_4$ compound results in a material that is inherently endowed with enhanced electrical conductivity compared to its pure form [18]. Furthermore, spherical nanoparticles of $NiMn_2O_4$ have been successfully synthesized through a straightforward and cost-effective method. Electrodes constructed from these monophasic spinel nanoparticles exhibit outstanding electrochemical performance and a high capacitance [19]. These findings provide further motivation for exploring potential capacitive applications of $NiCo_2O_4$/CoO in future research.

The implementation of hydrogen as a clean fuel source has driven research and development of new materials toward electrolytic water splitting, where competent electrocatalysts will increase the efficiency and economic viability of hydrogen production [20]. Some catalysts are based on iridium and ruthenium oxide, which is an expensive and scarce material. The idea of replacing these expensive catalysts has been based on $NiCo_2O_4$/CoO, thus providing a reduction in the costs associated with hydrogen production through water splitting. The problem is that its low electrical conductivity makes it difficult to apply on a large scale. To improve this limitation, $NiCo_2O_4$/CoO graphitic carbon is incorporated into the samples [20] to improve and optimize the synthesis techniques in obtaining the $NiCo_2O_4$. Moreover, the supercapacitive performances of $NiCo_2O_4$-based materials are primarily governed by the abundant faradaic redox reactions occurring in alkaline electrolytes, which stem from the presence of nickel and cobalt ions [21].

The exceptional electrical conductivity exhibited by binary oxides in contrast to simple metals has sparked significant interest. Among these binary metal oxides, including $NiCo_2O_4$, $MnCo_2O_4$ and $ZnCo_2O_4$, derived from cobalt oxide, $NiCo_2O_4$ stands out with its superior electrical conductivity compared to Co_3O_4 and NiO, while also demonstrating lower electrical resistance than NiO and CoO. Notably, the literature indicates that the introduction of citric acid induces notable variations in the morphology, crystallinity, porosity and electrical conductivity of $NiCo_2O_4$, further emphasizing its potential for exploration and optimization in various applications [22].

Table 1. Material used for sample preparation.

Molar concentration variation	$Ni_2NiO_6 \cdot 6H_2O$ (g)	$Co(NO_3)_2 \cdot 6H_2O$ (g)	$C_6H_8O_7H_2O$ (g)	H_2O (mL)
$Co_{3-x}Ni_xO_4$-Ni 1% wt.	0.158			
$Co_{3-x}Ni_xO_4$-Ni 4% wt.	0.654	15.716	1.85	60
$Co_{3-x}Ni_xO_4$-Ni 10% wt.	1.616			
$Co_{3-x}Ni_xO_4$-Ni 16% wt.	2.991			

This study synthesized a series of $NiCo_2O_4$/CoO and $NiCo_2O_4$/Co_3O_4 heterostructures using the sol-gel technique, with nickel doping levels ranging from 1% to 16%. Subsequently, the samples underwent a final thermal treatment at 1000 °C. Comprehensive characterization was performed using X-ray diffraction (XRD), transmission electron microscopy (TEM) and Fourier-transform infrared spectroscopy (FTIR) to investigate the impact of nickel doping on cobalt oxide and nickel cobaltite. The results demonstrate the coexistence of nickel cobaltite and cobalt oxide phases within the heterostructures. FTIR analysis revealed two absorption bands with slight shifts, indicating perturbations in the metal-oxygen bonds attributed to the doping effect. Moreover, TEM measurements confirmed the presence of the $NiCo_2O_4$/CoO interface. This research focused on investigating the structural and optical characteristics of $NiCo_2O_4$-based materials to obtain crystalline systems from a simplified and cost-effective approach, typically acquired through more complex methods. It is essential to provide

evidence that $NiCo_2O_4$/CoO systems are potential candidates for application as viable materials for supercapacitor electrodes, being the synthesis method crucial to purity control and production viability.

2. Materials and methods

The synthesis of $Co_{3-x}Ni_xO_4$, x = 0.01, 0.04, 0.1 and 0.16 was carried out using $Co(NO_3)_2{\cdot}6H_2O$ and citric acid $C_6H_8O_7{\cdot}H_2O$ as precursors, and distilled water as solvent. First, the solution was homogenized through magnetic stirring for 1 h at 60 ℃. Subsequently, nickel nitrate hexahydrate $N_2NiO_6{\cdot}6H_2O$ was added in the percentages shown in Table 1 with constant stirring. Next, the gel formed, was dried for 4 h at 80 ℃. Finally, the resultant product was subjected to heat treatment in a Hobersal brand muffle furnace at 400 ℃ for 3 h.

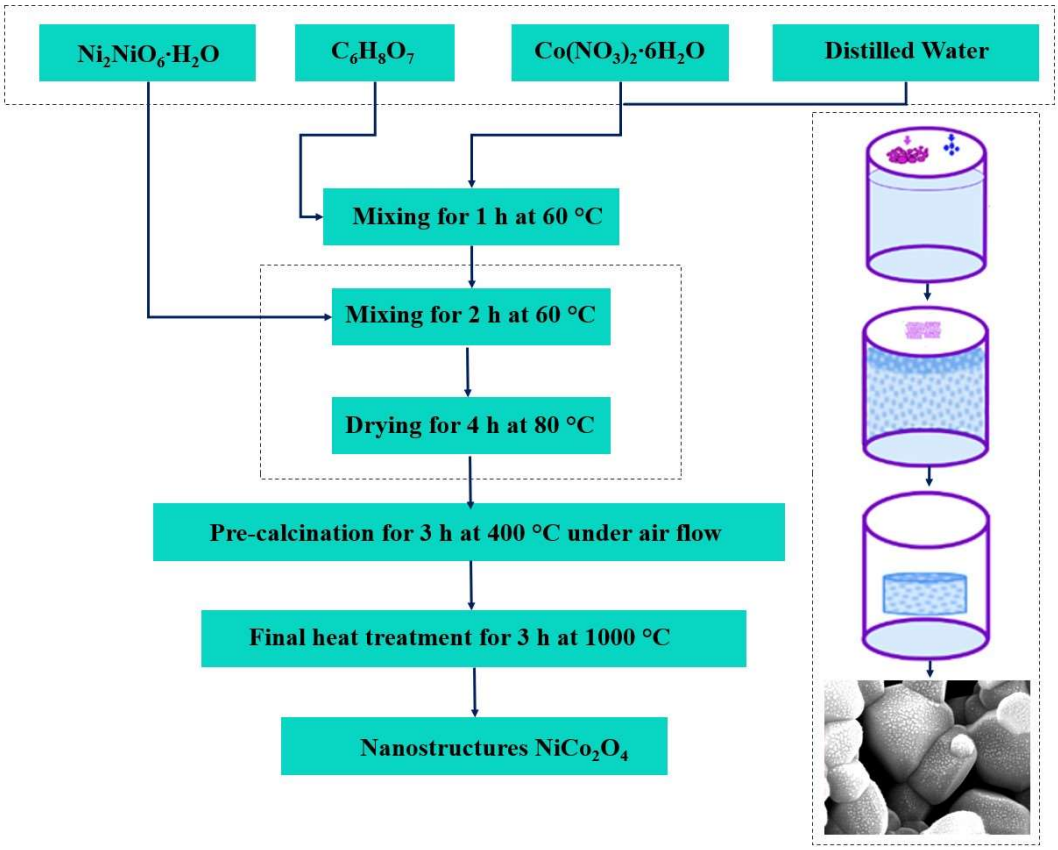

Figure 1. Schematic diagram of the sol-gel process in the $NiCo_2O_4$ preparation.

The samples obtained were sintered in a Carbolite brand oven at a temperature of 1000 ℃. The general scheme of the synthesis is observed in Figure 1. XRD measurements were performed on the PanAlytical X'Pert Pro equipment with analysis of Cu-Kα radiation. Data were collected at a 2θ angle between 10 and 90° under the Bragg Brentano mode. Scanning electron microscopy imagens were captured with the FESEMA JEDL J-7100 microscope. FTIR measurements were made on the Perkin-Elmer Spectrum Two FT-IR spectrometer equipment.

3. Results and discussion

The simulation of the nickel cobaltite structure is observed in Figure 2. In general, it is considered that $NiCo_2O_4$ adopts a spinel-like structure, where nickel occupies the octahedral sites and cobalt is distributed in the octahedral and tetrahedral sites [23]. Additionally, abundant redox couples (Ni^{2+}/Ni^{3+} and Co^{2+}/Co^{3+}) in $NiCo_2O_4$ can provide sufficient active sites, thus leading to good electrochemical/catalytic performance [24].

Figure 3a,b shows the compound obtained by calcining the cobalt samples with the addition of nickel. In Figure 3a, nickel was added at 1% and 4%. In this case, at an annealing of 1000 °C, the $NiCo_2O_4$/CoO phases appear. In the $NiCo_2O_4$ phase we have the crystallographic reference powder diffraction file (PDF) 01-073-1702 of the space group Fd-3m with the planes (hkl), (111), (220), (311), (222), (400), (331), (422), (511), (440), (531), (442), (620), (533), (622) and (444) corresponding to peaks in 2θ at 18.92, 31.15, 36.70, 38.40, 44.63, 48.88, 55.40, 59.11, 64.96, 68.33, 69.44, 73.80, 77.00, 78.06 and 82.25°, respectively, and inter planar spacing d (Å): 4.68, 2.86, 2.44, 2.34, 2.02, 1.86, 1.65, 1.56, 1.43, 1.37, 1.35, 1.28, 1.23, 1.22 and 1.17, respectively. The XRD patterns of the CoO oxide shown are: (111), (200), (220), (311) and (222) of the Bragg planes that are consistent with the fcc-CoO phase structure.

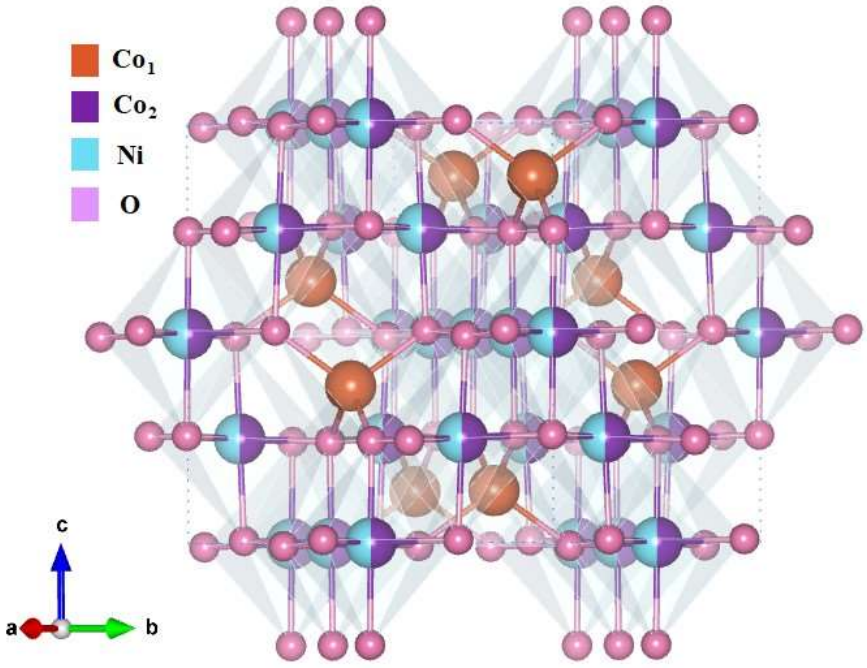

Figure 2. Simulation of the $NiCo_2O_4$ phase structure.

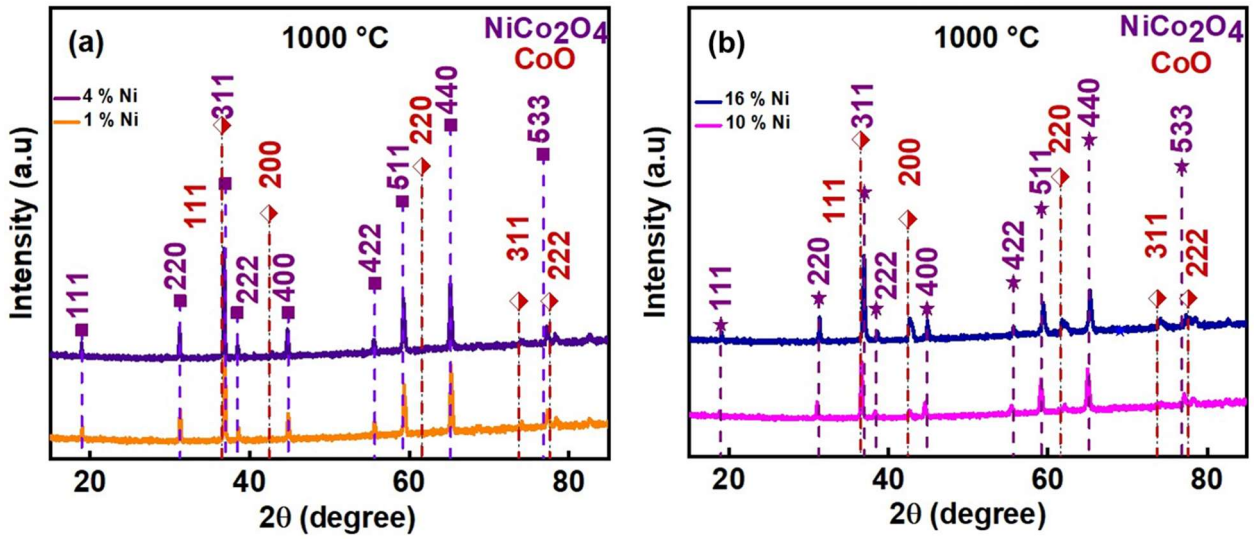

Figure 3. XRD patterns $NiCo_2O_4$/CoO with nickel doping at (a) 1%, 4%, and (b) 10%, 16%, calcination temperature 1000 ℃.

Figure 3b shows the samples at 10% and 16% nickel and annealing at 1000 ℃. In this case, the $NiCo_2O_4$/CoO crystallographic planes can be indexed to the samples. Indicating that the addition of nickel contributes so that the samples remain in the $NiCo_2O_4$ and CoO phase at this temperature. The PDF reference for the $NiCo_2O_4$ phase is 01-073-1702 and for the CoO phase the PDF reference is 01-075-0533. The Miller indices and distances of the crystallographic planes for the $NiCo_2O_4$ phase can be seen from Figure 3a. For the CoO phase of space group Fm-3m and planes (hkl), (111), (200), (220), (311) and (222), the position of the peaks in 2θ are 36.64, 42.57, 61.77, 74.02 and 77.91° and inter planar spacing d (Å) is 2.45, 2.12, 1.50, 1.27 and 1.22, respectively. Note that this phase transition occurs between 900 and 1000 ℃ [25]. Therefore, it is likely that intermediate structures such as nickel cobaltite are formed, due to the synthesis processes and the precursors used [26].

In recent years the combination of compounds with different properties in a single material has become important due to the possibility of improving performance when compared to individual compounds. Heterostructures are systems in which materials of different compositions or structures divide a common interface [27]. These heterostructures give the possibility of controlling various important parameters in technology such as: energy band gaps (*Eg*), mobility of charge carriers, effective mass, among others. In the case of X-rays, a compound with two phases obtained by the insertion of nickel and the increase in annealing temperature of the samples can be observed. Heterostructures have some applications in different fields such as photocatalysis and gas sensors [28]. The application depends on the migration of charges at the connecting interface between the two materials. This migration of charges is given by the difference in chemical potentials of the electrons in the crystalline structure, represented by the Fermi level. In X-rays, heterostructures exhibit distinct lattice parameters, which result in additional diffraction peaks being observed in their diffractogram. These diffraction peaks correspond to the different materials that comprise the structure. This unique characteristic leads to controlled optical and electrical properties, which give them an advantage for use in electronic devices.

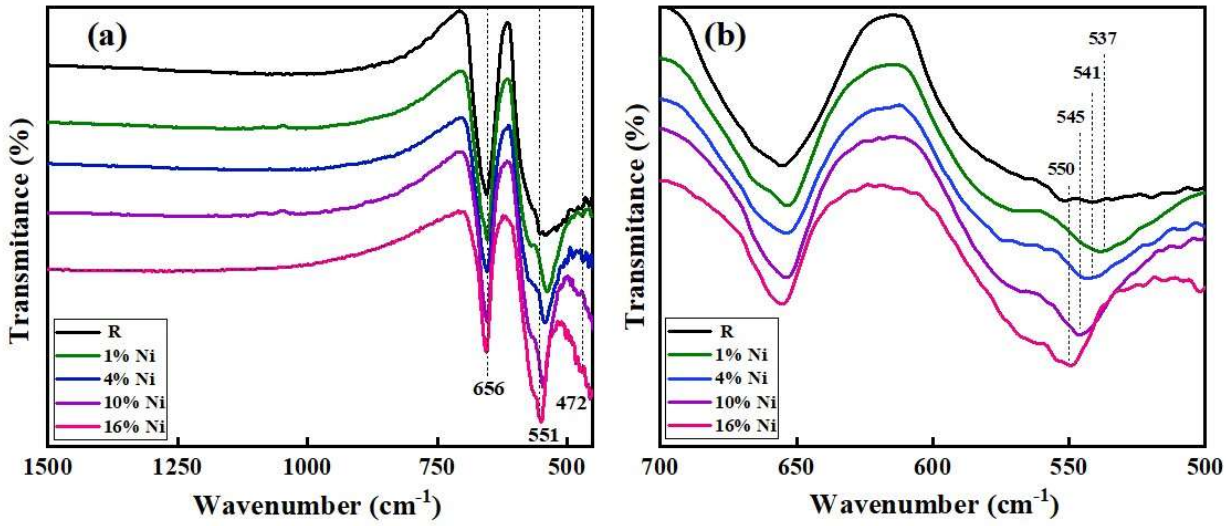

Figure 4. FTIR (a) spectra of $NiCo_2O_4$ samples with nickel doping at 1%, 4%, 10% and 16%, (b) magnification in the 700–500 cm^{-1} wavelength region.

Figure 4 shows the FTIR spectra of the $NiCo_2O_4$ samples doped with Ni at 1%, 4%, 10% and 16%. The results indicate two main absorption bands, ν_1 and ν_2, around 551 and 656 cm^{-1} for 1%, attributed to the vibration of the metal-oxygen bond. The absorption band ν_1 is related to the OB_3 vibrations in the spinel lattice B, which denotes the Co^{3+} ions in the octahedron structure, and to functionalization in the ABO_3 vibration with the Co^{2+} ions (octahedrons) [26,29].

Additionally, an absorptive factor is observed at 472 cm^{-1}, which is characteristic of NiO [30], and a slight change in the bands as a function of nickel doping. According to Gupta et al. [14], this is attributed to disturbances in the M–O (Ni–O, Co–O) bonds that generate the presence of oxygen vacancies. In Figure 4b, a shift is observed as a function of nickel doping, varying from 537 cm^{-1} for 1% Ni to 550 cm^{-1} for 16%. A vibration band is observed at 1044 cm^{-1}, which can be associated with the presence of the H–O–H vibration mode [31]. The shift observed in the peak between 537–550 cm^{-1} can be attributed to the structural deformation resulting from the incorporation of Ni atoms into the lattice. This alteration of the crystalline structure affects the chemical bonds, leading to a change in the frequency of molecular vibrations and, consequently, a shift in the peak position. The spectrum of the compound revealed the presence of two strong bands at low frequencies of 550 and 650 cm^{-1}. These observed peaks were strongly attributed to the stretching vibrations of the Ni–O (550 cm^{-1}) and Co–O bonds, respectively, in the nickel-cobalt oxide. It is inferred that there is interfacial charge transfer at the $NiCo_2O_4$/CoO interface. The presence of Ni atoms affects the chemical bonds by altering the frequency of molecular vibrations, which in turn affects the peak displacement. Shifts in the position of the FTIR peak can be indicative of changes in the chemical bonds present in the compound. In the case of the $NiCo_2O_4$/CoO compound, the presence of Ni atoms can affect the chemical bonding of CoO, potentially leading to a shift in the position of the FTIR peak.

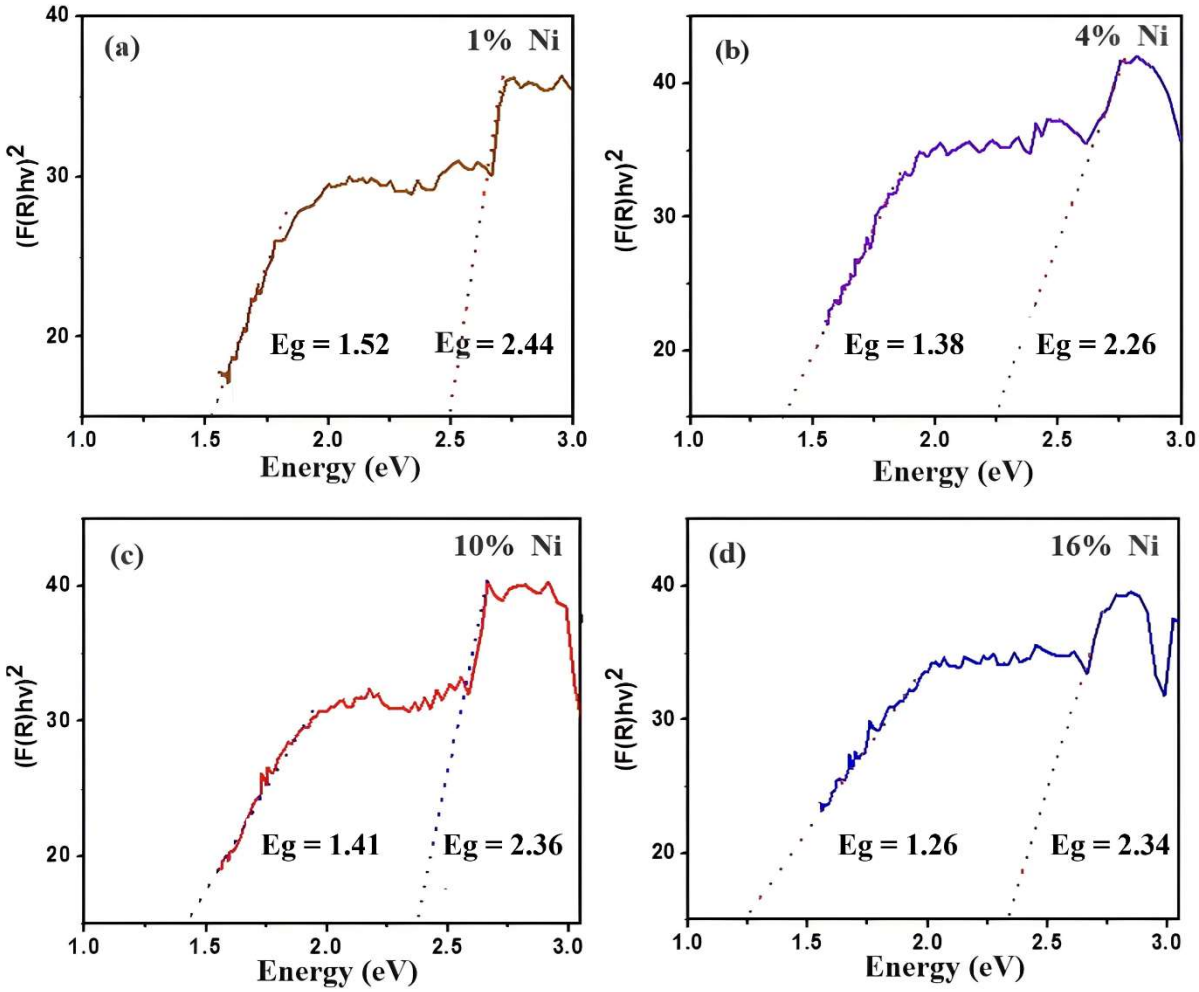

Figure 5. Diffuse reflectance spectra, obtained for $NiCo_2O_4$ samples with (a) 1%, (b) 4%, (c) 10% and (d) 16% Ni.

The optical properties were measured in the diffuse reflectance mode in the range of 330 to 700 nm and the optical E_g was calculated using the Tauc relationship with the following Eq 1:

$$F(r)hv = A(hv - E_g)^n \quad (1)$$

E_g represents the energy band gap, hv is the photon energy, A is the constant, $F(r)$ is the Kubelka-Munk function and n depends on the type of linked transition. The bandgap values are in the range of 1.82 and 2.03 eV for the first region, and 2.11 and 2.18 eV for the second one, as shown in Figure 5. This increase in the band gap value may be associated with doping due to a distortion in the lattice parameter and the insertion of nickel ions into the spinel matrix. In transition metals, the conduction and valence bands responsible for optical transitions involve high-density d-states. These 3d orbitals are divided into the tetrahedral and octahedral environments of oxygen, unlike the 4 and 4p orbitals that remain unchanged and result in solid optical transitions [32].

Figure 6 shows the scanning electron microscope (SEM) images of $NiCo_2O_4$ with nickel doping obtained at 1000 °C. The formation of semihexagonal particles with agglomerations and continuous stacking is evidenced. The growth mechanisms of the nanoparticles are associated with the synthesis method, and the sintering precursors and times. It is possible to establish that the aggregate growth

process and the oriented union of nanocrystals joined together produce various morphological structures [2]. The increase in temperature generates distributed grains with varied geometry and interconnected nanoparticles [33]. When the calcination temperature is high, very small, agglomerated nanoparticles are observed on the surface of a large particle [25].

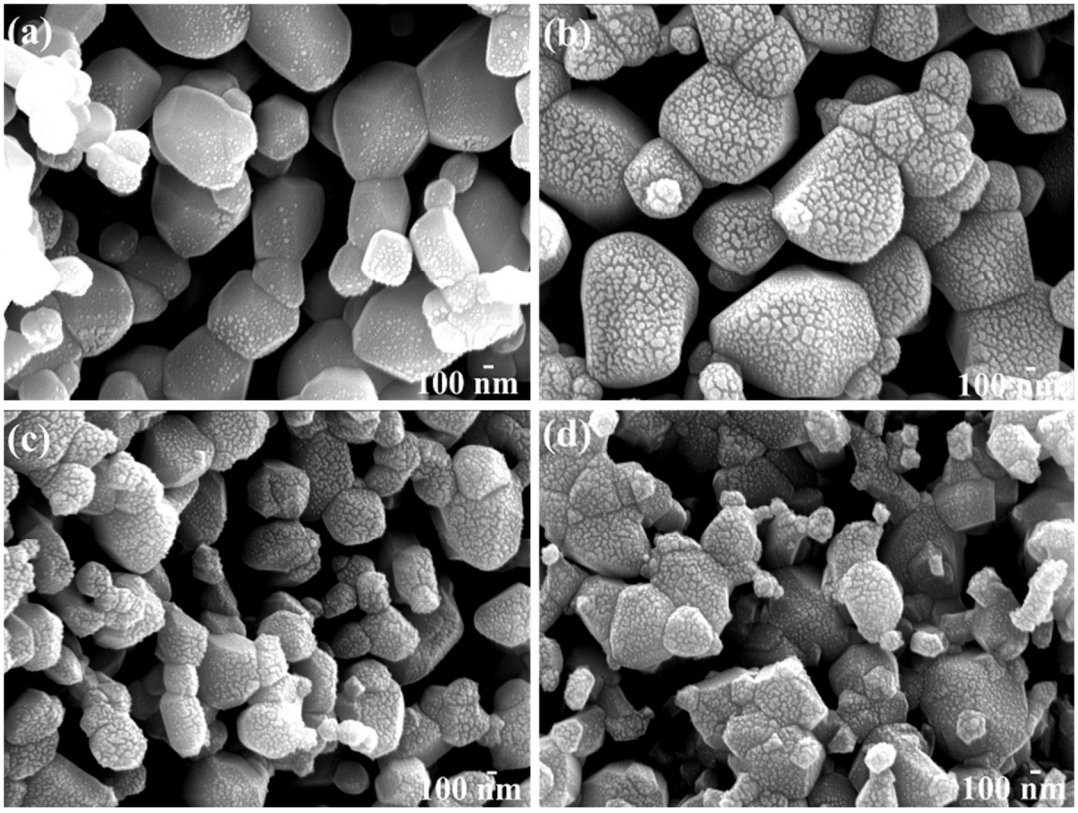

Figure 6. SEM micrographs of $NiCo_2O_4$ nickel doped samples: (a) 1%, (b) 4%, (c) 10% and (d) 16%.

The particle size is 376 and 269 nm for nickel doping at 1% and 16%, respectively, as shown in Figure 7. The final heat treatment temperature and the doping percentage influence the geometry and size of the particle [34]. The SEM images indicate that the synthesized material has an irregular morphology with a surface resembling an orange peel. The microparticles are of varying sizes, which may be attributed to their polycrystalline properties.

Upon careful observation of the morphology of samples containing 10% and 16% nickel, it is apparent that the grain size is smaller than that of samples with 4% nickel. However, two distinct grain sizes can be identified in the samples. One of these grain sizes is possibly attributed to the presence of $NiCo_2O_4$, while the other is likely due to the presence of CoO. Further investigation is necessary to confirm these findings and to determine the exact composition of each grain size. These results suggest that the addition of nickel can significantly impact the morphology of the material, leading to the formation of multiple grain sizes with different compositions.

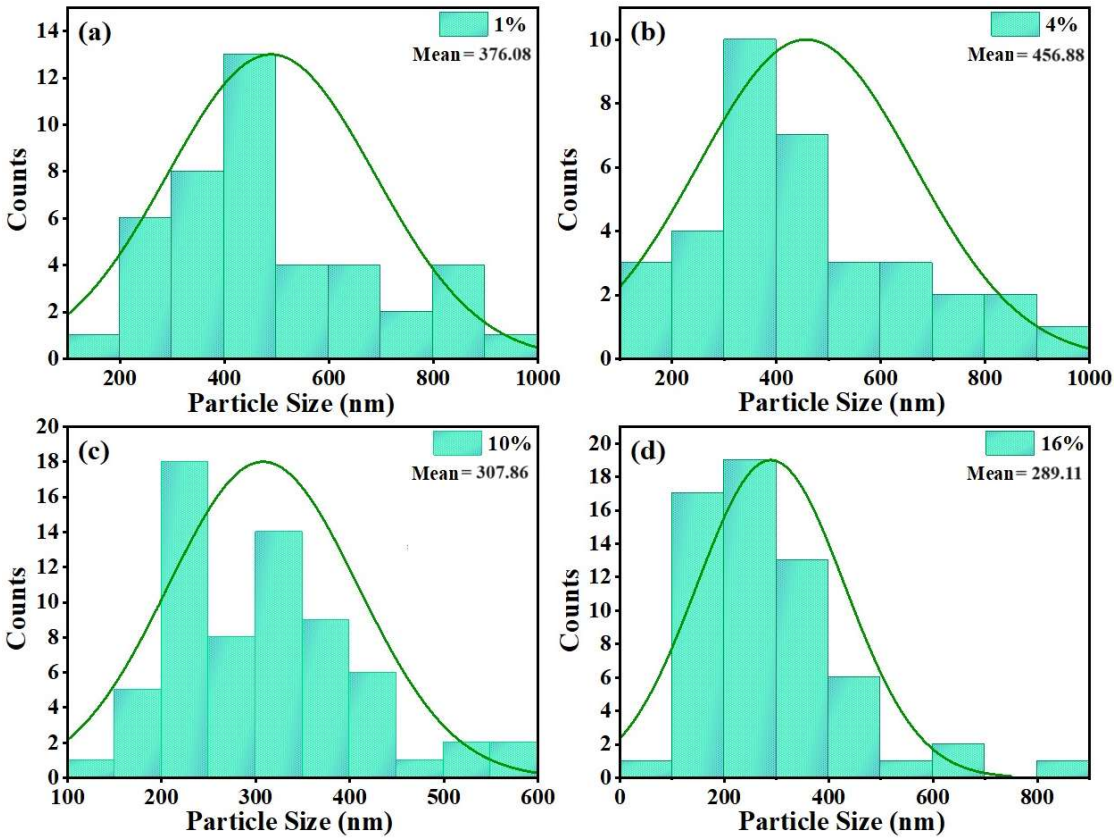

Figure 7. Particle size of $NiCo_2O_4$ samples doped with nickel at (a) 1%, (b) 4%, (c) 10% and (d) 16%.

The data presented in Figure 7 show that as the concentration of Ni increases, the particle size decreases. Specifically, at 16% Ni concentration, the particle size is 269 nm. This suggests that the formation of the $NiCo_2O_4$/CoO phases may be influenced by the concentration of Ni, leading to a decrease in particle size despite an increase in temperature. One possible explanation for this phenomenon is that as the percentage of Ni in the mixture increases, the formation of the $NiCo_2O_4$/CoO phases becomes more predominant.

These phases have a smaller particle size compared to other possible phases that can form at lower Ni concentrations, resulting in an overall decrease in particle size. It is also possible that the increase in temperature may lead to a higher degree of crystallinity, which would typically lead to larger particle sizes. However, in this case, the formation of the $NiCo_2O_4$/CoO phases may be overriding the effect of increased temperature on particle size. For more conclusive results, more detailed studies are needed. However, these results provide valuable insights into the role of Ni concentration in controlling the particle size and phase formation of $NiCo_2O_4$/CoO nanoparticles.

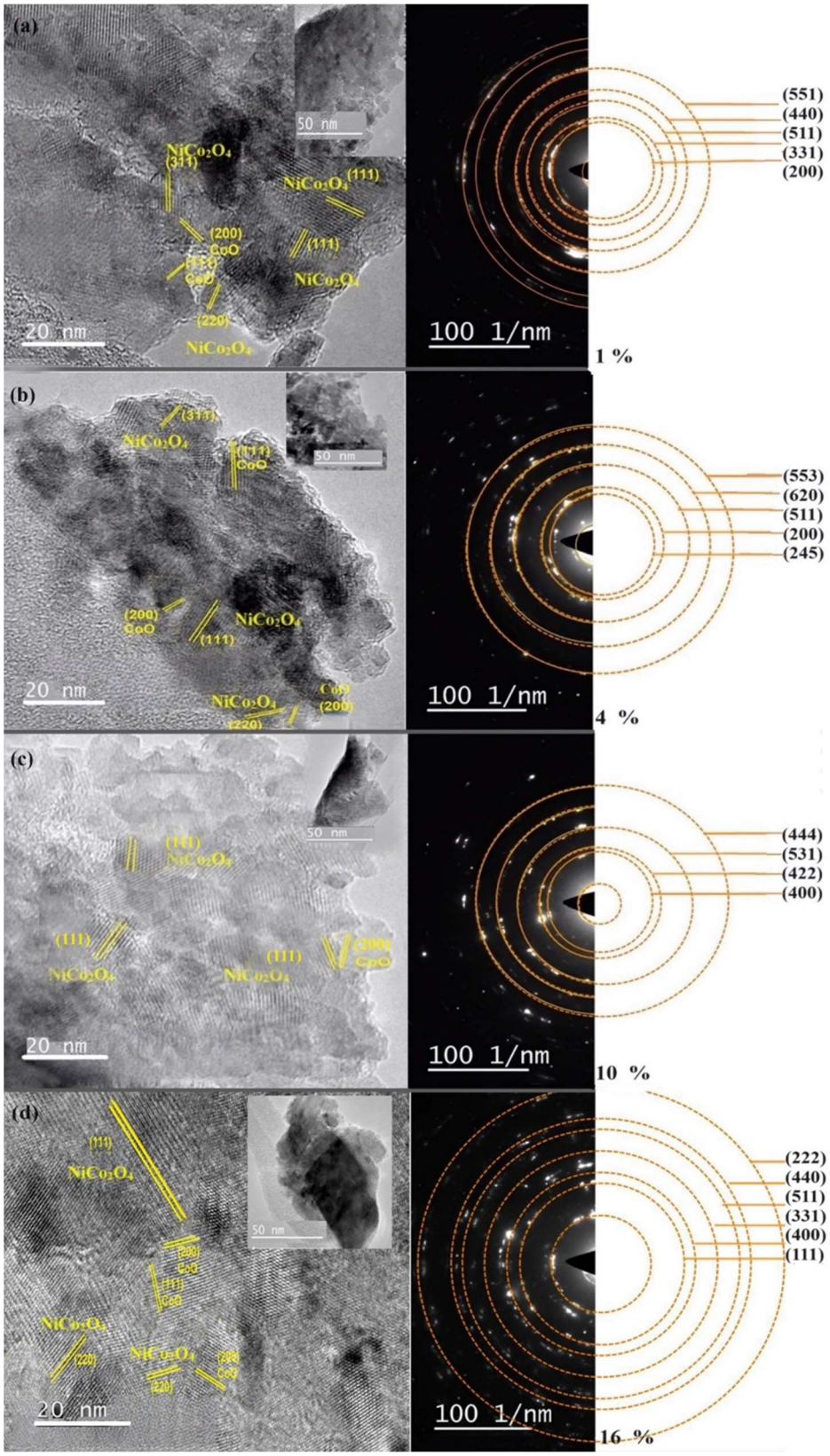

Figure 8. TEM, selected area electron diffraction (SAED), of $NiCo_2O_4$ samples doped with nickel at (a) 1%, (b) 4%, (c) 10% and (d) 16%.

In the analyzed samples it was possible to determine the proximity of the values of the interplanar distances in different crystallographic directions for the $NiCo_2O_4$ phase in the first two samples without being able to differentiate with Co_3O_4 since the interplanar distance is practically the same. However, in the 10% and 16% Ni samples, the crystallographic interplanar distances of $NiCo_2O_4$ and CoO were also found. Furthermore, the high-resolution transmission electron microscopy (HRTEM) image of $NiCo_2O_4$ shows a clear lattice structure, as shown in Figure 8. The fringe spacing of the lattice corresponds to the crystal planes of $NiCo_2O_4$. SAED analysis shows rings of corresponding lattice planes, implying a polycrystalline $NiCo_2O_4$/CoO characteristic. All observed rings are well indexed with characteristic $NiCo_2O_4$/CoO planes that are related to XRD.

Based on the HRTEM image in Figure 8a, it is evident that there exists an interface between the (200) plane of CoO and the (311) and (220) planes of $NiCo_2O_4$ in the heterostructures, particularly for the sample with 1% Ni composition. Such interfaces often serve as active sites, contributing to the unique properties of these heterostructures.

Furthermore, the HRTEM image in Figure 8b provides additional information about the surfaces of the samples, specifically $NiCo_2O_4$ and CoO. Notably, a discernible grain boundary is observed between the $NiCo_2O_4$ and CoO regions within the structure. The interplanar spacing of 0.461 nm is indexed to the (111) lattice plane of $NiCo_2O_4$, while 0.278 and 0.240 nm correspond to the (220) and (311) lattice planes, respectively, of the cubic phase of $NiCo_2O_4$. On the other hand, within the zone, the interplanar crystal spacing of 0.213 nm is indexed to the (200) lattice plane of CoO, and 0.246 nm corresponds to the (111) lattice plane of the CoO phase. In Figure 8c, the observed surface plans are (111) for $NiCo_2O_4$ and (200) for CoO. The distinct separation between the grains of each phase is clearly demarcated, as illustrated in the figure. Similarly, in Figure 8d, the identified plans are (200) for CoO and (111) and (220) for $NiCo_2O_4$, mirroring the previous case. The insets present in all of Figure 8 depict the particle sizes of each sample, which do not exceed 100 nm.

The HRTEM analysis of the heterostructures uncovers clear interfaces and crystal lattice planes, suggesting the existence of potential active sites at these interfaces, which could lead to promising applications in diverse fields. Figure 8 further illustrates the well-defined grain boundaries and relatively small particle sizes of $NiCo_2O_4$ and CoO, providing valuable structural insights into these materials.

4. Conclusions

$NiCo_2O_4$/CoO was synthesized via the sol-gel method, followed by calcination at 1000 °C. SEM analysis showed that higher levels of Ni doping resulted in smaller particle sizes, possibly due to increased formation of $NiCo_2O_4$/CoO phases. The synthesized material was found to consist of two well-defined grain sizes and two phases. Particle geometry and size were influenced by factors such as doping, temperature and synthesis method. The final heat treatment temperature had a significant effect on the morphological, vibrational and optical properties of the cobalt oxide samples, as well as the addition of Ni. SAED patterns revealed a polycrystalline nature with well-defined rings. Particle size distribution was uneven and changed as the amount of Ni increased. This low-cost synthesis method and temperature increase could be useful for obtaining these phases, which are important in the capacitor industry.

Use of AI tools declaration

The authors declare they have not used Artificial Intelligence (AI) tools in the creation of this article.

Acknowledgments

The authors thank the Universidad Nacional de Colombia Bogotá, EMBRAPA, SP, Sao Carlos Brasil, Centers Científics Tecnològics (CCiTUB) of the Universitat de Barcelona. Also, thanks to the University of America for giving author L.J. Cárdenas the time to write.

Conflict of interest

The authors declare no conflict of interest.

References

1. Wu Z, Zhu Y, Ji X (2014) $NiCo_2O_4$-based materials for electrochemical supercapacitors. *J Mater Chem A* 2: 14759–14772. https://doi.org/10.1039/C4TA02390K
2. Cheng P, Dang F, Wang Y, et al. (2021) Gas sensor towards n-butanol at low temperature detection: Hierarchical flower-like Ni-doped Co_3O_4 based on solvent-dependent synthesis. *Sens Actuators B Chem* 328: 129028. https://doi.org/10.1016/j.snb.2020.129028
3. Shepit M, Paidi VK, Roberts CA, et al. (2021) Unusual magnetism in $Cu_xCo_{3x}O$ nanoparticles. *Phys Rev B* 103: 024448. https://doi.org/10.1103/PhysRevB.103.024448
4. Wu B, Shan C, Zhang X, et al. (2021) CeO_2/Co_3O_4 porous nanosheet prepared using rose petal as biotemplate for photo-catalytic degradation of organic contaminants. *Appl Surf Sci* 543: 148677. https://doi.org/10.1016/j.apsusc.2020.148677
5. Li QP, Liu FQ, Mu XL, et al. (2021) Co_3O_4/CdS energy-storing nanocomposite: A promising photoanode for photoelectrochemical cathodic protection in the dark. *J Alloys Compd* 870: 159340. https://doi.org/10.1016/j.jallcom.2021.159340
6. V-Niño ED, Díaz Lantada A, Lonne Q, et al. (2018) Manufacturing of polymeric substrates with copper nanofillers through laser stereolithography technique. *Polymers* 10: 1325. https://doi.org/10.3390/polym10121325
7. Keerthana SP, Yuvakkumar R, Senthil Kumar P, et al. (2021) Influence of tin (Sn) doping on Co_3O_4 for enhanced photocatalytic dye degradation. *Chemosphere* 277: 130325. https://doi.org/10.1016/j.chemosphere.2021.130325
8. Abdallah AM, Awad R (2021) Sm and Er partial alternatives of Co in Co_3O_4 nanoparticles: Probing the physical properties. *Physica B* 608: 412898. https://doi.org/10.1016/j.physb.2021.412898
9. Li Q, Zhang Q, Zhou Z, et al. (2021) Boosting Zn-ion storage capability of self-standing Zn-doped Co_3O_4 nanowire array as advanced cathodes for high-performance wearable aqueous rechargeable Co//Zn batteries. *Nano Res* 14: 91–99. https://doi.org/10.1007/s12274-020-3046-8
10. Bao W, Li Y, Zhang J, et al. (2023) Interface engineering of the $NiCo_2O_4$@MoS_2/TM heterostructure to realize the efficient alkaline oxygen evolution reaction. *Int J Hydrogen Energy* 48: 12176–12184. https://doi.org/10.1016/j.ijhydene.2022.12.184
11. Zhou X, Li Y, Zhao J, et al. (2023) Tailoring the electronic structure of $NiMoO_4$ nanowires with $NiCo_2O_4$ nanosheets by constructing heterostructure interfaces for improving oxygen evolution reaction. *Ionics* 29: 1983–1990. https://doi.org/10.1007/s11581-023-04965-5
12. Bao W, Xiao L, Zhang J, et al. (2021) Electronic and structural engineering of $NiCo_2O_4$/Ti electrocatalysts for efficient oxygen evolution reaction. *Int J Hydrogen Energy* 46: 10259–10267. https://doi.org/10.1016/j.ijhydene.2020.12.126

13. Wu X, Zhou X, Hu L, et al. (2021) Porous $NiCo_2O_4$–$FeCo_2O_4$ nanowire arrays as advanced electrodes for high-performance flexible asymmetric supercapacitors. *Energ Fuel* 35: 12680–12687. https://doi.org/10.1021/acs.energyfuels.1c01517
14. Rashti A, Lu X, Dobson A, et al. (2021) Tuning MOF-derived Co_3O_4/$NiCo_2O_4$ nanostructures for high-performance energy storage. *ACS Appl Energy Mater* 4: 1537–1547. https://doi.org/10.1021/acsaem.0c02736
15. Chang Q, Liang H, Shi B, et al. (2021) Ethylenediamine-assisted hydrothermal synthesis of $NiCo_2O_4$ absorber with controlled morphology and excellent absorbing performance. *J Colloid Interf Sci* 588: 336–345. https://doi.org/10.1016/j.jcis.2020.12.099
16. Chen C, Su H, Lu L, et al. (2021) Interfacing spinel $NiCo_2O_4$ and NiCo alloy derived N-doped carbon nanotubes for enhanced oxygen electrocatalysis. *Chem Eng J* 408: 127814. https://doi.org/10.1016/j.cej.2020.127814
17. Cardenas-Flechas LJ, Barba-Ortega J, Joya MR (2020) Copper and iron oxide films deposited in titanium nanotubes. *Rev UIS Ing* 19: 171–178. https://doi.org/10.18273/revuin.v19n1-2020016
18. Sivakumar P, Vikraman D, Raj CJ, et al. (2021) Hierarchical NiCo/NiO/$NiCo_2O_4$ composite formation by solvothermal reaction as a potential electrode material for hydrogen evolutions and asymmetric supercapacitors. *Int J Energy Res* 45: 19947–19961. https://doi.org/10.1002/er.7065
19. Wu Z, Zhu Y, Ji X (2019) Study on charge storage mechanism in working electrodes fabricated by sol-gel derived spinel $NiMn_2O_4$ nanoparticles for supercapacitor application. *Appl Surf Sci* 463: 513–525. https://doi.org/10.1016/j.apsusc.2018.08.259
20. Srinivasa N, Shreenivasa L, Adarakatti PS, et al. (2019) In situ addition of graphitic carbon into a $NiCo_2O_4$/CoO composite: Enhanced catalysis toward the oxygen evolution reaction. *RSC Adv* 9: 24995–25002. http://dx.doi.org/10.1039/C9RA05195C
21. Li Y, Han X, Yi T, et al. (2019) Review and prospect of $NiCo_2O_4$-based composite materials for supercapacitor electrodes. *J Energy Chem* 31: 54–78. https://doi.org/10.1016/j.jechem.2018.05.010
22. Manalu A, Tarigan K, Humaidi S, et al. (2022) Synthesis, microstructure and electrical properties of $NiCo_2O_4$/rGO composites as pseudocapacitive electrode for supercapacitors. *Int J Electrochem Sci* 17: 22036. https://doi.org/10.20964/2022.03.11
23. Peres APS, Lima AC, Barros BS, et al. (2012) Synthesis and characterization of $NiCCo_2O_4$ spinel using gelatin as an organic precursor. *Mater Lett* 89: 36–39. https://doi.org/10.1016/j.matlet.2012.08.044
24. Zhao N, Yang F, Zhao C, et al. (2021) Construction of pH-dependent nanozymes with oxygen vacancies as the high-efficient reactive oxygen species scavenger for oral-administrated antiinflammatory therapy. *Adv Healthc Mater* 10: e2101618. https://doi.org/10.1002/adhm.202101618
25. Cardenas-Flechas LJ, Freire PTC, Paris EC, et al. (2021) Temperature-induced structural phase transformation in samples of Co_3O_4 and $Co_{3-x}Ni_xO_4$ for CoO. *Materialia* 18: 101155. https://doi.org/10.1016/j.mtla.2021.101155
26. Marco JF, Gancedo JR, Gracia M, et al. (2001) Cation distribution and magnetic structure of the ferrimagnetic spinel $NiCo_2O_4$. *J Mater Chem* 11: 3087–3093. https://doi.org/10.1039/B103135J
27. Wang P, Jia C, Huang Y, et al. (2021) Van der waals heterostructures by design: From 1D and 2D to 3D. *Matter* 4: 552–581. https://doi.org/10.1016/j.matt.2020.12.015
28. Liu Y, Fang Y, Yang D, et al. (2022) Recent progress of heterostructures based on two dimensional materials and wide bandgap semiconductors. *J Phys: Condens Matter* 34: 183001. https://doi.org/10.1088/1361-648x/ac5310

29. Lakehal A, Bedhiaf B, Bouaza A, et al. (2018) Structural optical and electrical properties of Ni-doped Co_3O_4 prepared via sol-gel technique. *Mat Res* 21: 1–7. https://doi.org/10.1590/1980-5373-MR-2017-0545
30. Cardenas-Flechas LJ, Xuriguera Martín E, Padilla Sanchez JA, et al. (2021) Experimental comparison of the effect of temperature on the vibrational and morphological properties of $Ni_xCo_{3-x}O_4$ nanostructures. *Mater Lett* 303: 130477. https://doi.org/10.1016/j.matlet.2021.130477
31. Shen G, Chen PC, Ryu K, et al. (2009) Devices and chemical sensing applications of metal oxide nanowires. *J Mater Chem* 19: 828–839. https://doi.org/10.1039/B816543B
32. Thota S, Kumar A, Kumar J (2009) Optical electrical and magnetic properties of Co_3O_4 nano crystallites obtained by thermal decomposition of sol-gel derived oxalates. *Mater Sci Eng B* 164: 30–37. https://doi.org/10.1016/j.mseb.2009.06.002
33. Liu MC, Kong LB, Lu C, et al. (2012) A sol–gel process for fabrication of $NiO/NiCo_2O_4/Co_3O_4$ composite with improved electrochemical behavior for electrochemical capacitors. *ACS Appl Mater Interfaces* 4: 4631–4636. https://doi.org/10.1021/am301010u
34. Cardenas-Flechas LJ, Raba Paes AM, Joya MR (2020) Synthesis and evaluation of nickel doped Co_3O_4 produced through hydrothermal technique. *DYNA* 87: 184–191. https://doi.org/10.15446/dyna.v87n213.84410